

COVER PAGE

Document downloaded by @DAEL

Sat Nov 28 03:09:32 2026
For personal use

When automatic English translation is provided, only the original document is authentic.
The EAA cannot be held responsible of any translation error

Bibliographical reference

Imaging Cracks in Bones Using Acoustic Nonlinearity: A Simulation Study, Yang Liu, Xiasheng Guo, Zhao Da, Dong Zhang and Xiufen Gong, Acta Acustica **vol. 97** (Number 5), 2011, pp. 728-733

DOI
https://doi.org/10.3813/AAA.918452

ACTA ACUSTICA UNITED WITH ACUSTICA
Vol. 97 (2011) 728 – 733
DOI 10.3813/AAA.918452

Imaging Cracks in Bones Using Acoustic Nonlinearity: A Simulation Study

Yang Liu, Xiasheng Guo, Zhao Da, Dong Zhang, Xiufen Gong
Institute of Acoustics, Key Laboratory of Modern Acoustics (Nanjing University), Ministry of Education, Nanjing University, Nanjing 210093, China. dzhang@nju.edu.cn

Summary
This article proposes an acoustic nonlinear approach combined with the time reversal technique to image cracks in long bones. In this method, the scattered ultrasound generated from the crack is recorded, and the third harmonic nonlinear component of the ultrasonic signal is used to reconstruct an image of the crack by the time reversal process. Numerical simulations are performed to examine the validity of this approach. The fatigue long bone is modeled as a hollow cylinder with a crack of 1, 0.1, and 0.225 mm in axial, radial and circumferential directions respectively. A broadband 500 kHz ultrasonic signal is used as the exciting signal, and the extended three-dimensional Preisach-Mayergoyz model is used to describe the nonclassical nonlinear dynamics of the crack. Time reversal is carried out by using the filtered third harmonic component. The localization capability depends on the radial depth of the crack.

PACS no. 43.25.Dc, 43.35.Yb, 43.80.Vj

1. Introduction

Micro-damage in bones, also termed as fatigue damage, is commonly caused from daily cyclic loading, which exists in the form of micro-cracks (typically 10 µm to 1 mm long) in normal bones in humans and animals in vivo [1]. The presence of micro-cracks reduces the elastic modulus of the bone [2, 3, 4], as well as bone strength [5]. Although living bone has the ability to repair and remodel fatigue cracks [6, 7] to prevent bone failure, micro-cracks may grow under loading to cause bone fractures, known as 'stress fractures' [8, 9, 10, 11]. There are millions of micro-cracks in the bone. Due to the remodeling ability of bone, the micro-cracks are safe in most situations. But if the micro-cracks grow to mm scale, they become dangerous and may have a big chance to cause failure. As a result, finding the dangerous fatigue crack is important in clinical diagnosis.

The currently used techniques for the diagnosis of bone fragility, such as x-ray densitomoetric techniques and linear quantitative ultrasound techniques [12], are based on the measurement of bone mineral density (BMD). However, micro-damage mainly affects the mechanical properties of the bone rather than BMD, thus these techniques are relatively insensitive to micro-damage of the bone. For assessment of fatigue damage in bone, two techniques are commonly used, i.e. staining techniques [13] and optical techniques [14]. However, both are limited to the measurement of in vitro specimens.

Received 10 October 2010,
accepted 29 May 2011.

It has been known that micro-cracks in fatigued materials could induce localized hysteretic deformation [15]. This behavior has been characterized as nonclassical nonlinearity. Nonlinear resonant ultrasound spectroscopy (NRUS) [16] and nonlinear wave modulation spectroscopy (NWMS) [17] techniques have been successfully applied to study the micro-damage in human bones. Both techniques reveal the integral quantity of bone damage: resonance frequency shift in NRUS and side band energy in NWMS are used to assess bone damage level. However, NRUS and NWMS do not give any information about the damage location.

Time reversal (TR) provides a means of focusing waves back on the source on the assumption of time reversal invariance [18]. In TR acoustics, an array of transducers (time reversal mirror) records the wavefield coming from the source and sends back its time-reversed version in the medium. As time reversal invariance is guaranteed by the wave equation in a non-dissipative medium, the reemitted field is expected to retrofocus on the source and reconstruct the signal. This technique has been developed in various fields of applications including medicine [19], geophysics [20], underwater acoustics [21] and nondestructive testing [22]. Recently, combined with elastic nonlinearity, two techniques, i.e., TREND (time reversed elastic nonlinearity diagnostic), and TR-NEWS (time reversed nonlinear elastic wave spectroscopy) have been proposed for isolating a nonlinear scatter such as a crack in a solid for nondestructive testing [23]. TREND uses TR as a tool for energy focusing to illuminate the nonlinear scatter [24, 25], while TR-NEWS uses TR for nonlinear source identification [26, 27, 28, 29, 30].

© S. Hirzel Verlag · EAA

Most previous studies of TR simulation using the PM approach, deal with 2D plates in the applications of NDE. The purpose of this study is to develop an acoustic nonlinear approach for localization of cracks in long bones. This is the first TR simulation study in a pipe- like bone model, which is performed in the 3D cylindrical coordinates. As bones with micro-cracks have been proved to display non-classical nonlinear response [16], we combine this nonlinearity with TR NEWS to localize the cracks in the bone. To examine the this approach, a three-dimensional (3D) numerical model is developed for describing nonlinear response from the bone with a dangerous crack of mm scale in its length. Nonlinear based TR ultrasound is used to localize the crack. In addition, the effect of the radial depth of the crack on the localization capability is discussed.

2. Theory and methods

2.1. Elastic wave propagation in circular tubes using a finite-difference approach

Fatigue-induced fractures are most found in tibia, femur, humerus and ulna, all of which are limbs and can be approximately regarded as circular tubes in geometry. To do an elementary study, we model the bone as a long isotropic circular tube. The approach proposed by Gsell [31] is adopted to carry out the 3D simulation of linear elastic wave propagation in tubes.

Wave propagation in isotropic elastic solids is governed by the well-known Navier equation,

$$\left(\lambda+\mu\right)\nabla\nabla\cdot\boldsymbol{u}+\mu\nabla^2\boldsymbol{u}+\rho\boldsymbol{f}=\rho\frac{\partial^2\boldsymbol{u}}{\partial t^2}, \tag{1}$$

where λ and μ are the Lamé constants, $\boldsymbol{u}$ is the displacement vector and ρ is the mass density, while $\boldsymbol{f}$ denotes the external excitation applied on the solid body. With respect to the radial, axial and circumferential displacement components (i. e., u_r, u_z and u_j), equation (1) in cylindrical coordinates could be decomposed to three coupled partial differential equations, which are discretized using second order central differences in time and space. For instance, the second-order time derivatives of u_i are discretized as

$$\frac{\partial^2 u_i}{\partial t^2}=\frac{1}{\Delta t^2}\left(u_i^{n+1}-2u_i^n+u_i^{n-1}\right),\quad i=r,\varphi,z, \tag{2}$$

in which Δt is the time increment and n is the index of the time. More detailed discretization rules could be found in [31].

The considered cylindrical tube is uniformly meshed in radial, axial and circumferential directions. The three displacement components are allocated on a staggered grid [31]. For the purpose of discretization calculations of boundary nodes, a layer of nodes next to the surfaces outside the tube is also introduced, the type of which is the same as that inside the tube [31]. To ensure the stability and convergence of FDTD calculations, the largest element size satisfies the following inequality [31],

$$\frac{\lambda_{\min}}{\max\left(\Delta r,\Delta\varphi,r_{\max},\Delta z\right)}>8, \tag{3}$$

where $\lambda_{\min}$ is the shortest wavelength. The time step is also restricted, and the criteria in cylindrical coordinates proposed by Chen and Chew [32] is adopted,

$$\Delta t\, c_{\max}\sqrt{\frac{1}{\Delta r^2}+\frac{1}{(r_{\min}\Delta\varphi)^2}+\frac{1}{\Delta z^2}}\le 1. \tag{4}$$

For the boundary conditions, both ends of the tube are fixed, while the inner and outer surfaces are stress-free except for the region covered by the transmitter.

2.2. Modeling of the crack with PM model

In this study, only the non-classical nonlinearity induced by the crack is considered, while the impact of other micro-cracks and the classical nonlinearity in the bone are ignored. As a result, the intact area is modeled using linear dynamics, while the crack is modeled with hysteretic nonlinear dynamics. The Presach-Mayergoyz (PM) model [33] is adopted to describe the hysteretic nonlinear behavior. The implementation of the PM model is based on a multiscale approach developed by Van Den Abeele [34]. In the one dimensional (1D) case, the elementary hysteretic element used in the PM model is featured by two characteristic threshold stresses τ_c and τ_o ($\tau_c>\tau_o$), corresponding to two states called "closed" and "open" respectively. Depending on weather the stress grows over τ_c or decreases below τ_o, the element is in "closed" or "open" state. In a crack, each cell of the FDTD calculation grid consists of a number of elementary elements. The strain ε of the cell is governed by the stress τ, and is dependent on the stress history. The bulk modulus K of one cell is given by [34]

$$\frac{1}{K}=\frac{1}{E(1+\beta\tau+\delta\tau^2)}+\hat{\gamma}\frac{\mathrm{d}f_c(\tau)}{\mathrm{d}\tau}, \tag{5}$$

where E is the linear elastic modulus, β and δ are the classical quadratic and cubic nonlinear parameters which are zero here, $\hat{\gamma}$ is the hysteretic strain contribution of an individual mesoscopic cell when all hysteretic elements are in "closed" state. The function $f_c(t)$ describes the fraction of hysteretic elements in the "closed" state at the stress τ in one cell.

To implement the PM model in 3D numerical simulations, it is required to extend the scalar model to vector fields. When considering the wave propagation in a 3D isotropic solid medium, the stress-strain relation could be described using Einstein's summation convention,

$$\tau_{ij}=C_{ijkl}\varepsilon_{kl}. \tag{6}$$

The elastic tensor C_{ijkl} should be decomposed to the orthogonal unit-direction bases in PM space. For a 3D isotropic solid, the eigenvectors correspond to six eigenstress/eigenstrain vectors. It has been indicated that the eigenstrain vector is perfectly collinear with the corre-

sponding eigenstress vector [35].

$$\hat{\varepsilon}^{(1)} = \begin{pmatrix} 1 \\ 1 \\ -2 \\ 0 \\ 0 \\ 0 \end{pmatrix}, \quad \hat{\varepsilon}^{(2)} = \begin{pmatrix} 1 \\ -1 \\ 0 \\ 0 \\ 0 \\ 0 \end{pmatrix}, \quad \hat{\varepsilon}^{(3)} = \begin{pmatrix} 1 \\ 1 \\ 1 \\ 0 \\ 0 \\ 0 \end{pmatrix},$$

$$\hat{\varepsilon}^{(4)} = \begin{pmatrix} 0 \\ 0 \\ 0 \\ 1 \\ 0 \\ 0 \end{pmatrix}, \quad \hat{\varepsilon}^{(5)} = \begin{pmatrix} 0 \\ 0 \\ 0 \\ 0 \\ 1 \\ 0 \end{pmatrix}, \quad \hat{\varepsilon}^{(6)} = \begin{pmatrix} 0 \\ 0 \\ 0 \\ 0 \\ 0 \\ 1 \end{pmatrix}. \tag{7}$$

The eigenvalue corresponding to $\hat{\varepsilon}^{(1)}$ is $3\lambda + 2\mu$, while the other five are all equal to 2μ. Projected on each direction of eigenvectors, the stress-strain relation becomes scalar, which is convenient to implement nonlinearity. For example, in the direction of $\hat{\varepsilon}^{(1)}$, the projected stress and strain have the relation as

$$\tau_1 = K_1 \varepsilon_1, \tag{8}$$

in which $K_1 = 3\lambda + 2\mu$. Nonlinearity could be implemented by applying equation (5) to K_1. For simplicity, hysteretic nonlinearity is applied in all six directions in this study, while in reality the stress-strain relation could be directional.

During the FDTD calculations, the stiffness of an eigenstate in each direction is described using the associated PM space. Thus, at every time step, the stresses are projected in each direction to update the equivalent elastic coefficients, and then calculate the new displacements, which are essential for solving new stress components in the next time step. When a sinusoid signal is input, stress-strain hysteretic response distorts the waveform and generates nonlinear components.

2.3. TR NEWS technique

Due to the nonlinearity of the crack, the received signal in the model contains nonlinear components. In TRNEWS technique, only the nonlinear components of the received signals are time reversed and reemitted in the model. In order to reemit the nonlinear components of the signal, two filtering methods are commonly used, i.e. the bandpass filter and the pulse inversion filtering [26]. In this study, the third harmonic is extracted from the received signal using a Butterworth bandpass filter. The third harmonic component is chosen as the detected signal since the non-classical nonlinearity exhibits stronger odd harmonics [36].

After collection of the received displacement components in all three directions, the TR NEWS technique is then carried out to localize crack according to the following procedures: (1) The third harmonic component is filtered from the received nonlinear signal generated by the crack; (2) the filtered signal is reversed in the time domain and sent back to the model as the excitation signal at the location where the signal was recorded; (3) localization of the crack from the recorded displacement information.

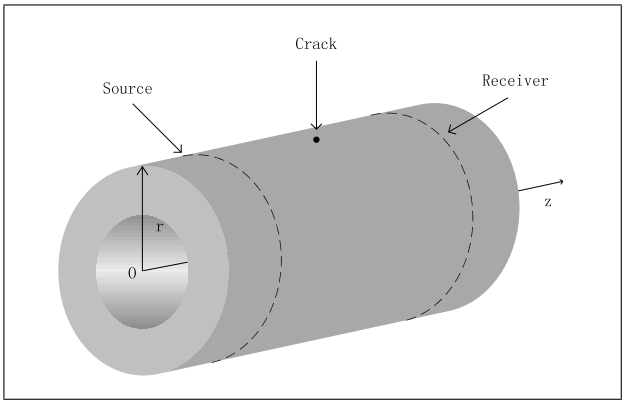

Figure 1. Illustration of a crack embedded in a long bone; the bone is modeled as a tube with length 200 mm, inner radii 4.5 mm and outer radii 8.5 mm.

3. Results

To examine this approach, a single crack configuration case is studied. As shown in Figure 1, the long bone is modeled as a 20 cm long isotropic circular tube with inner and outer radii of 4.5 and 8.5 mm. The intact bone material is considered isotropic with compression and shear velocities of $c_L = 4063$ m/s and $c_T = 1846$ m/s. The density of the material is $\rho = 1500\,\mathrm{kg/m^3}$ and the attenuation is not considered in this model. These values correspond to the isotropic bone properties [37]. A crack is located in the middle of the tube in the axial direction, 2 mm underneath the outer surface of the tube. The dimensions of the crack are set to be 1, 0.1, 0.225 mm in axial, radial and circumferential direction respectively. A PM space model with uniform distribution of τ_c and τ_o is used, that is $\rho(\tau_c, \tau_o) = 1$ between ± 5 MPa and $\rho(\tau_c, \tau_o) = 0$ everywhere else, for a maximum strain 0.001. The hysteresis parameter $\hat{\gamma}$ is $2 \cdot 10^{-4}$. It is a uniform distribution of the same level for all six components. An annular transmitter of 5 mm width is located at $z = 2$ cm on outer surface of the tube, applies forced displacement in radial direction. Displacement signals are recorded for 200 µs by 180 receiver units of an annular array located at the $z = 18$ cm on the outer surface of the tube. The signal used for excitation is a tone-burst consisting 6 sinusoidal cycles at a central frequency of 500 kHz. Lower frequency is not chosen as the resolution power is limited. The wave amplitude is modulated using a Hanning function, $0.5(1-\cos(2\pi t/W))$, here W denotes the width of the window.

3.1. Localization of the crack

Figure 2a shows the distribution of u_r as a function of z and φ of a mid-cylindrical plane ($r = 6.5$ mm) which intersect the crack. The time of Figure 2a is 142.8 µs, which corresponds to the maximum of the signal at the focusing point. The focusing effect is not observed due to the overwhelming domination of non-focusing waves. It could be explained by the dispersive nature of the waves traveling in the pipe-like structure. As the waves have multiple modes with different velocities, a very long length of the

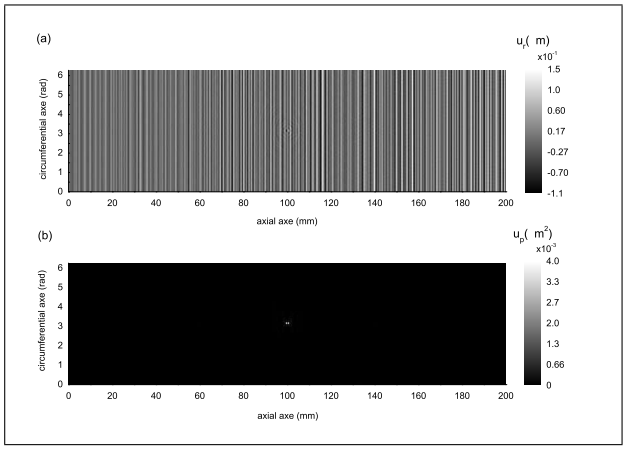

Figure 2. Reconstructed distribution of u_r on the mid-cylindrical plane ($r = 6.5$ mm): (a) initial image and (b) post-processed image.

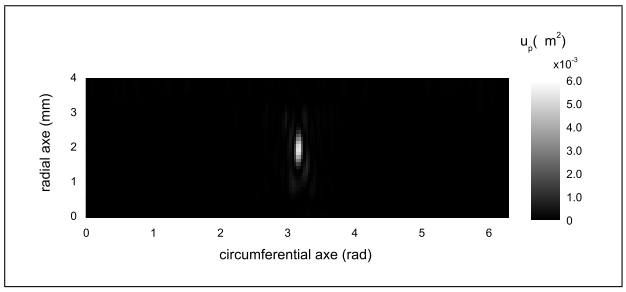

Figure 3. Reconstructed distribution of u_z on the $r - \varphi$ plane at $z = 10$ cm.

recorded signal is required to make a perfect time reversal. A simple post-processing method is proposed here to improve the quality for visualization with the relatively short length of signals. Due to the axis-symmetric excitation, the non-focusing waves are axis-symmetric. The data for every circumferential line are substituted with the square of the subtraction with the corresponding mean values. The post-processing values are re-plotted in Figure 2b, where the position and size of the defect could be obviously determined. This focused spot coincides with the position of the crack we have set in the model, which demonstrates the capability of this approach to localize the crack in the bone.

To test the sensitivity in the radial direction, Figure 3 shows the distribution u_z on the $r - \varphi$ plane located at $z = 10$ cm. Compared with Figure 2b, the image is not clear and the previous locatation of the crack can not be determined. This can be explained by the fact that the dimension of the crack in the radial direction, compared with the wavelength, is much smaller than that in the axial direction.

3.2. Effect of the radial depth of the crack

As only the received signals in the outer surface can be used for imaging in real configuration, we also discuss the effect of the radial position of the crack on the localization capability. The dimensions of the cracks are the same

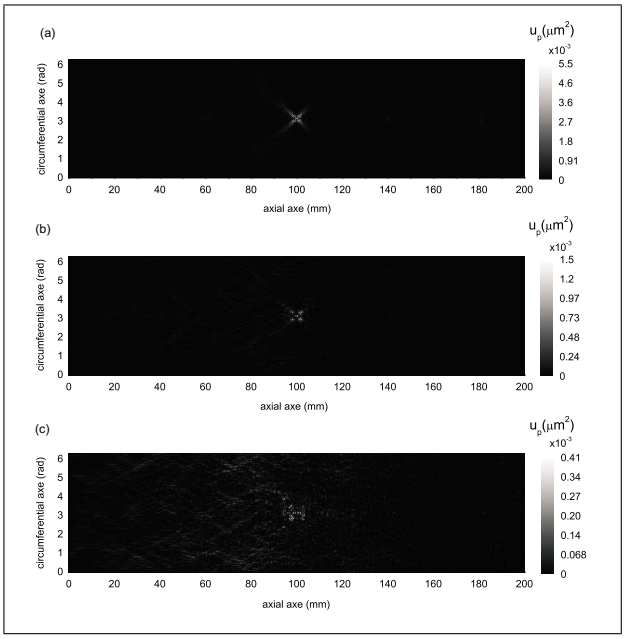

Figure 4. Distribution of u_r on the outer surface for crack located at various radial positions: (a) 1 mm, (b) 1.5 mm and (c) 2 mm.

as shown in Figure 1, while the positions of cracks in the radial direction are set to be 1, 1.5, 2, 2.5, and 3 mm underneath the outer surface, respectively.

Figure 4 gives the typical reconstructed images, where (a), (b) and (c) correspond to the cracks located at 1, 1.5 and 2 mm underneath the outer surface, respectively. It is obvious that the localization capability becomes better as the crack is close to the outer surface. In this study two parameters $A_1 = \max(A^1_{\text{crack}}/A^1_{\text{intact}})$ and $A_2 = \max(\overline{A^2_{\text{crack}}}/\overline{A^2_{\text{intact}}})$ are defined to quantitatively evaluate the localization capability, where $\overline{A^1_{\text{crack}}}$ represents the mean value of the absolute amplitude of u_r in the region of upright projective area of the crack in the outer surface; $\overline{A^1_{\text{intact}}}$ represents the mean value of the absolute amplitudes of u_r in the residual area of the outer surface; $\overline{A^2_{\text{crack}}}$ represents the mean value of the absolute amplitude of u_r in the region of the crack in the mid-cylindrical plane (r = radial depth); $\overline{A^2_{\text{intact}}}$ represents the mean value of the absolute amplitudes of u_r in the residual area of the mid-cylindrical plane. The maximum argument means the maximum value over time, which corresponds to the focusing time. Table I lists the values of the parameter A_1 and A_2 for the cracks at various radial depths.

Both parameters A_1 and A_2 represent the contrast of the crack to the intact area, where A_1 and A_2 are calculated from received and generated intensities, respectively. It is observed that the larger radial depth leads to the lower A_1 and A_2, which suggests the degradation of localization capability. Noting that the cases for radial depths at 2.5 and 3 mm are some different from this behavior, which can be explained by that generated intensity becomes higher as the crack is close the inner boundary. Fink [38] indicated that multiple reflections on the guide interfaces sig-

Table I. Effect of the radial depth of crack on the localization capability.

Depth	A_1	A_2	A_1/A_2
1.0 mm	17.95	44.94	0.399
1.5 mm	9.14	35.51	0.257
2.0 mm	4.01	22.63	0.177
2.5 mm	2.87	31.19	0.092
3.0 mm	2.99	39.56	0.076

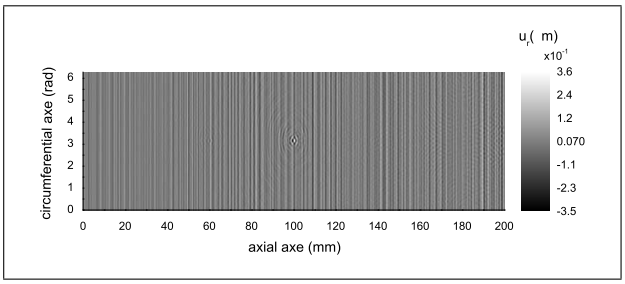

Figure 5. Reconstructed results of u_r on the outer surface with 2D receiver.

nificantly increase the apparent aperture of the TR mirror, as the reflecting boundaries can act as one part of the TR transducers. The localization capability is related to the defect position towards the TR transducers and the boundaries [29]. In this table, another parameter A_1/A_2 is also calculated as the received intensity from unitary emitted intensity. The use of A_1/A_2 could reduce the effect of boundary, and is observed to decrease as the crack's radial depth increases.

4. Discusssion

As indicated by Figure 2a, recording signal without an adequate length cannot refocus very well by time reversal. This could be explained by the lack of "coda" used for the time reversal. Extending the length of the recorded signals could improve the refocus quality. On the other hand, we examine if increasing the information in space used for the time reversal can improve the quality. We perform a time reversal using 2D array receivers by increasing the receivers in radial direction, which are positioned at the same distance in a surface perpendicular to the axial direction, same distance to the end of the tube as the 1D array. Figure 5 gives the results obtained by a 2D array. Comparing with Figure 2a obtained from a 1D array, it is obvious that Figure 5 shows the better refocusing capability. It suggests that recording information in more dimensions is benefit to achieve good refocusing for a 3D time reversal problem. In comparsion, good refocusing results can also be achieved by using 1D array combined with our simple post-processing method. It is noted that this signal post-processing method should satisfy the condition of axisymmetric wave propagation. When the excitation is not axis-symmetrical, asymmetrical flexural modes occur in the tube. Besides, due to the dispersive nature of the guided wave, different guided wave modes can propagate in the tube. Their reactions with the crack are different. Combining the different wave modes with the nonlinear time reversal is not included in this paper.

This study provides a preliminary study of an approach for crack localization in long bones. The 3D configuration of bone considered here is still far from realistic: (1) Bone material is inhomogeneous and usually contains voids. Besides, millions of micro-cracks exist in the bone, which might contribute to the nonclassical nonlinearity. Fortunately, TR has shown its capabilities of compensating for refraction, mode conversion and anisotropy. TR could also reduce the speckle noise generated from random microstructures like the micro- cracks in the bone [38]. Furthermore, the contribution of the voids will be excluded in the reconstructed image since the voids exhibit no nonlinear response [39]. (2) This study only considers the non-classical nonlinearity induced by the cracks, while ignores the impact of other micro-cracks and the classical nonlinearity in the bone. The third harmonic generated by the classical nonlinearity does not prevent the field reproduction [40]. When the signals retransmit into the medium in the TR process, the harmonics ($N > 1$) transfer energy back to the fundamental frequency as the time waveform reverses back to its original sinusoidal shape. As a result, the third harmonic generated from the classical nonlinearity would vanish in the TR process (3) Though mm-size cracks are considered in this study, a distribution of micro-cracks region of a few cm^2 also behaves as a damage region, presenting non-classical nonlinearity.

5. Conclusions

This study proposes a numerical study for imaging cracks in bone by use of nonlinear acoustics combining with time reversal technique. The fatigue bone is modeled by a 3D long bone model with a crack, and the nonclassical nonlinear dynamics of the crack is described by the extended three-dimensional PM model. Nonlinear based TR ultrasound is used to image the crack. Results demonstrate the capability of this approach for localization of cracks in bone-like material. However, the localization quality in the outer surface is affected by the radial depth of the crack. Furthermore, the acoustic attenuation should be considered in future study.

Acknowledgement

The work is supported by National Basic Research Program 973 (Grant No. 2011CB707900) from Ministry of Science and Technology, China, National Natural Science Foundation of China (No. 10974093), and the Fundamental Research Funds for the Central Universities (Nos. 1103020402 and 1112020401).

References

[1] J. G. Hazenberg, D. Taylor, T. C. Lee: Mechanisms of short crack growth at constant stress in bone. Biomaterials **27** (2006) 2114–2122.

[2] M. Schaffler, E. L. Radin, D. B. Burr: Mechanical and morphological effects of strain rate on fatigue of compact bone. Bone **10** (1989) 207–214.

[3] E. F. Wachtel, T. M. Keaveny: Dependence of trabecular damage on mechanical strain. Journal of Orthopaedic Research **15** (1997) 781–787.

[4] P. Zioupos: Accumulation of in-vivo fatigue microdamage and its relation to biomechanical properties in ageing human cortical bone. J. Microsc. **201** (2001) 270–278.

[5] D. B. Burr, M. R. Forwood, D. P. Fyhrie, R. B. Martin, M. B. Schaffler, C. H. Turner: Bone microdamage and skeletal fragility in osteoporotic and stress fractures. J. Bone. Miner. Res. **12** (1997) 6–15.

[6] R. B. Martin: A theory of fatigue damage accumulation and repair in cortical bone. Journal of Orthopaedic Research **10** (1992) 818–825.

[7] D. B. Burr, R. B. Martin, M. B. Schaffler, E. L. Radin: Bone remodeling in response to in vivo fatigue microdamage. Journal of Biomechanics **18** (1985) 189–200.

[8] X. Wang, G. L. Niebur: Microdamage propagation in trabecular bone due to changes in loading mode. Journal of Biomechanics **39** (2006) 781–790.

[9] D. B. Burr: Bone exercise and stress fractures. Exerc. Sport Sci. Rev. **25** (1997) 171–94.

[10] B. R. Beck: Tibial stress injuries: an aetiological review for the purposes of guiding management. Sports Med. **26** (1998) 265–79.

[11] S. W. Donahue, N. A. Sharkey, K. A. Modanlou, L. N. Sequeira, R. B. Martin: Bone strain and microcracks at stress fracture sites in human metatarsals. Bone **27** (2000) 827–33.

[12] C. C. Gluer, R. Barkmann: Quantitative ultrasound: use in the detection of fractures and in the assessment of bone composition. Current Osteoporosis Report **1** (2003) 98–104.

[13] F. J. O'Brien, D. Taylor, T. C. Lee: An improved labelling technique for monitoring microcrack growth in compact bone. J. Biomech. **35** (2002) 523–526.

[14] X. Wang, D. B. Masse, H. J. Leng, K. P. Hess, R. D. Ross, R. K. Roeder, G. L. Niebur: Detection of trabecular bone microdamage by micro-computed tomography. Journal of Biomechanics **40** (2007) 3397–3340.

[15] W. L. Morris, O. Buck, R. V. Inman: Acoustic harmonic generation due to fatigue damage in high-strength aluminum. J. Appl. Phys. **50** (1979) 6737–6741.

[16] M. Muller, R. Guyer, M. Talmant, P. Laugier, P. A. Johnson: Nonlinear resonant ultrasound spectroscopy (NRUS) applied to damage assessment in bone. J. Acoust. Soc. Am. **118** (2005) 3946–3952.

[17] T. J. Ulrich, P. A. Johnson, R. A. Guyer: Interaction dynamics of elastic waves with a complex nonlinear scatterer through the use of a time reversal mirror. Physical Review Letters **98** (2007) 104301–4.

[18] M. Fink: Time reversal of ultrasonic fields. I, II and III. IEEE Trans. Ultrason. Ferroelectr. Freq. Control **39** (1992) 555–592.

[19] J. L. Thomas, F. Wu, M. Fink: Time reversal focusing applied to lithotripsy. Ultrason. Imaging **18** (1996) 106–121.

[20] J. Tromp, C. Tape, Q. Liu: Seismic tomography, adjoint methods, time reversal and banana-doughnut kernels. Geophys. J. Int. **160** (2005) 195–216.

[21] W. A. Kuperman, W. S. Hodgkiss, H. C. Song, T. Akal, C. Ferla, D. R. Jackson: Phase conjugation in the ocean: Experimental demonstration of an acoustic time-reversal mirror. J. Acoust. Soc. Am. **103** (1998) 25–40.

[22] N. Chakroun, M. Fink, F. Wu: Time reversal processing in nondestructive testing. IEEE Trans. Ultrason. Ferroelectr. Freq. Control **42** (1995) 1087–1098.

[23] T. J. Ulrich, A. Sutin, R. A. Guyer, P. A. Johnson: Time reversal and nonlinear elastic wave spectroscopy (TR NEWS) techniques. Int. J. Nonlinear Mech. **43** (2008) 209–216.

[24] T. J. Ulrich, P. A. Johnson, A. Sutin: Imaging nonlinear scatterers applying the time reversal mirror. J. Acoust. Soc. Am. **119** (2006) 1514–1518.

[25] A. Sutin, J. A. TenCate, P. A. Johnson: Development of nonlinear time reversed acoustics (NLTRA) for applications to crack detection in solids. Proceedings of the 5th World Congress on Ultrasonics, 2003, 121–124.

[26] A. S. Gliozzi, M. Griffa, M. Scalerandi: Efficiency of time-reversed acoustics for nonlinear damage detection in solids. J. Acoust. Soc. Am. **120** (2006) 2506–2517.

[27] T. J. Ulrich, P. A. Johnson, M. Müller, D. Mitton, M. Talmant, P. Laugier: Application of nonlinear dynamics to monitoring progressive fatigue damage in human cortical bone. Applied Physics Letters **91** (2007) 213901–3.

[28] T. Goursolle, S. Callé, S. Dos Santos, O. Bou Matar: A two-dimensional pseudospectral model for time reversal and nonlinear elastic wave spectroscopy. J. Acoust. Soc. Am. **122** (2007) 3220–3229.

[29] T. Goursolle, S. Dos Santos, O. Bou Matarb, S. Callé: Nonlinear based time reversal acoustic applied to crack detection: simulations and experiments. International Journal of Non-Linear Mechanics **43** (2008) 170–177.

[30] B. E. Anderson, M. Griffa, C. Larmat, T. J. Ulrich, P. A. Johnson: Time reversal. Acoust. Today **4** (2008) 5–16.

[31] D. Gsell, T. Leutenegger, J. Dual: Modeling three-dimensional elastic wave propagation in circular cylindrical structures using a finite-difference approach. J. Acoust. Soc. Am. **116** (2004) 3284–3293.

[32] Y. H. Chen, W. C. Chew: A three-dimensional finite difference code for the modeling of sonic logging tools. J. Acoust. Soc. Am. **103** (1998) 702–712.

[33] K. McCall, R. Guyer: Equation of state and wave propagation in hysteretic nonlinear elastic materials. J. Geophys. Res. **99** (1994) 23887–23897.

[34] K. Van Den Abeele, F. Schubert, V. Aleshin, F. Windels, J. Carmeliet: Resonant bar simulations in media with localized damage. Ultrasonics **42** (2004) 1017–1024.

[35] K. Helbig, P. N. J. Rasolofosaon: A theoretical paradigm for describing hysteresis and nonlinear elasticity in arbitrary anisotropic rocks. Proceedings of the Ninth International Workshop on Seismic Anisotropy, Society of Exploration Geopysicistry, Tulsa, 2000.

[36] G. Zumpano, M. Meo: A new nonlinear elastic time reversal acoustic method for the identification and localisation of stress corrosion cracking in welded plate-like structrues - a simulation study. Int. J. Nonlinear Mech. **44** (2007) 3666–3684.

[37] V. C. Protopappas, I. C. Kourtis, K. N. Malizos, C. V. Massalas, D. I. Fotiadis: Three-dimensional finite element modeling of guided ultrasound wave propagation in intact and healing long bones. J. Acoust. Soc. Am. **121** (2007) 3907–3921.

[38] M. Fink, D. Cassereau, A. Derode, C. Prada, P. Roux, M. Tanter, J. Thomas, F. Wu: Time-reversed acoustics. Rep. Prog. Phys. **63** (2000) 1933–1995.

[39] P. A. Johnson: The new wave in acoustic testing. Mater. World **7** (1999) 544–546.

[40] K. B. Cunningham, M. F. Hamilton, A. P. Brysev, L. M. Krutyansky: Time reversed sound beams of finite amplitude. J. Acoust. Soc. Am. **109** (2001) 2668–2674.

[41] R. de Rosny, M. Fink: Overcoming the diffraction limit in wave physics using a time-reversal mirror and a novel acoustic sink. Phys. Rev. Lett. **89** (2002) 124301.